

# Harvesting Hot Holes in Plasmon-Coupled Ultrathin Photoanodes for High-Performance Photoelectrochemical Water Splitting

Ehsan Vahidzadeh,\* Sheng Zeng, Kazi M. Alam, Pawan Kumar, Saralyn Riddell, Narendra Chaulagain, Sergey Gusarov, Alexander E. Kobryn, and Karthik Shankar\*

Cite This: *ACS Appl. Mater. Interfaces* 2021, 13, 42741–42752

Read Online

ACCESS |

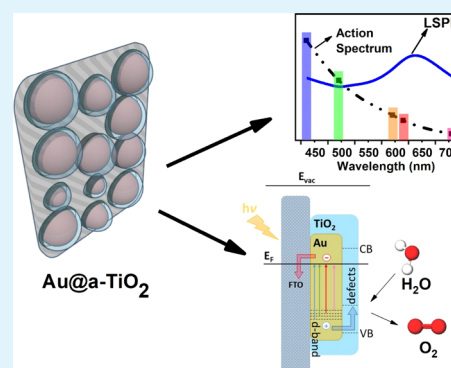
Metrics & More

Article Recommendations

Supporting Information

**ABSTRACT:** The harvesting of hot carriers produced by plasmon decay to generate electricity or drive a chemical reaction enables the reduction of the thermalization losses associated with supra-band gap photons in semiconductor photoelectrochemical (PEC) cells. Through the broadband harvesting of light, hot-carrier PEC devices also produce a sensitizing effect in heterojunctions with wide-band gap metal oxide semiconductors possessing good photostability and catalytic activity but poor absorption of visible wavelength photons. There are several reports of hot electrons in Au injected over the Schottky barrier into crystalline TiO<sub>2</sub> and subsequently utilized to drive a chemical reaction but very few reports of hot hole harvesting. In this work, we demonstrate the efficient harvesting of hot holes in Au nanoparticles (Au NPs) covered with a thin layer of amorphous TiO<sub>2</sub> (a-TiO<sub>2</sub>). Under AM1.5G 1 sun illumination, photoanodes consisting of a single layer of ~50 nm diameter Au NPs coated with a 10 nm shell of a-TiO<sub>2</sub> (Au@a-TiO<sub>2</sub>) generated 2.5 mA cm<sup>-2</sup> of photocurrent in 1 M KOH under 0.6 V external bias, rising to 3.7 mA cm<sup>-2</sup> in the presence of a hole scavenger (methanol). The quantum yield for hot-carrier-mediated photocurrent generation was estimated to be close to unity for high-energy photons ( $\lambda < 420$  nm). Au@a-TiO<sub>2</sub> photoelectrodes produced a small positive photocurrent of 0.1 mA cm<sup>-2</sup> even at a bias of -0.6 V indicating extraction of hot holes even at a strong negative bias. These results together with density functional theory modeling and scanning Kelvin probe force microscope data indicate fast injection of hot holes from Au NPs into a-TiO<sub>2</sub> and light harvesting performed near-exclusively by Au NPs. For comparison, Au NPs coated with a 10 nm shell of Al<sub>2</sub>O<sub>3</sub> (Au@Al<sub>2</sub>O<sub>3</sub>) generated 0.02 mA cm<sup>-2</sup> of photocurrent in 1 M KOH under 0.6 V external bias. These results underscore the critical role played by a-TiO<sub>2</sub> in the extraction of holes in Au@a-TiO<sub>2</sub> photoanodes, which is not replicated by an ordinary dielectric shell. It is also demonstrated here that an ultrathin photoanode (<100 nm in maximum thickness) can efficiently drive sunlight-driven water splitting.

**KEYWORDS:** plasmonic photocatalysis, FDTD electromagnetic simulations, spontaneous dewetting, artificial photosynthesis, interband damping



## 1. INTRODUCTION

The production of solar fuels using semiconductor photocatalysts and photoelectrodes has been investigated since the early 1970s.<sup>1,2</sup> Photochemically stable, catalytically active semiconductors such as TiO<sub>2</sub>, SrTiO<sub>3</sub>, GaN, g-C<sub>3</sub>N<sub>4</sub>, and so forth have wide band gaps and therefore primarily harvest blue and ultraviolet photons while wasting (through lack of absorption) a large number of lower energy photons capable of driving chemical reactions of interest such as H<sub>2</sub> generation from water and photoreduction of CO<sub>2</sub> into value-added hydrocarbons. Moderate band gap and narrow band gap semiconductors such as Cu<sub>2</sub>O, Si, GaP, CdS, and so forth experience photocorrosion, and some even have poor catalytic activity. Another inherent problem associated with semiconductor catalysts is the thermalization loss associated with the relaxation of more energetic charge carriers excited by

supra-band gap photons to the bottom of the conduction band before participating in desired redox processes.

Recently, there has been increasing interest in plasmonic catalysis to circumvent these limitations.<sup>3–7</sup> Plasmonic catalysis offers the potential of driving a wide variety of chemical reactions close to room temperature by harnessing the intense light-matter interaction, fast charge transfer, and strong vibrational coupling to adsorbates exhibited by select plasmonic nanoparticles (NPs). Plasmonic catalysis can be predominantly carrier-driven or phonon-driven. NPs, made of

Received: June 8, 2021

Accepted: August 25, 2021

Published: September 3, 2021



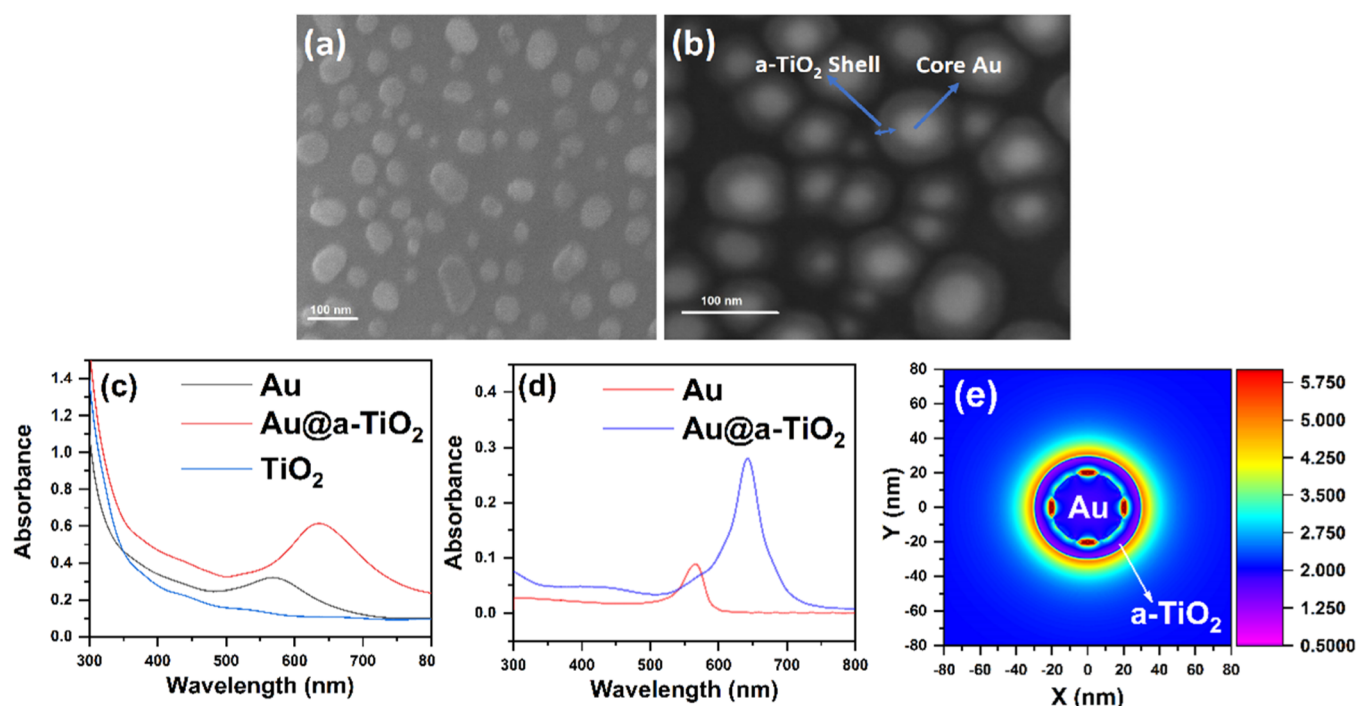


**Figure 1.** Helium ion images of (a) Au and (b) Au@TiO<sub>2</sub> on the glass substrate. (c) UV-vis spectrum of Au, a-TiO<sub>2</sub>, and Au@a-TiO<sub>2</sub> and (d) FDTD-simulated absorption cross-section of Au and Au@a-TiO<sub>2</sub>. (e) Top-view electric field profile of Au@a-TiO<sub>2</sub> under 650 nm excitation. The scale bar in Figure 1e represents the amplitude of the local electric field.

a select group of materials that includes Ag, Au, Cu, Al, and certain transition-metal nitrides, exhibit localized surface plasmon resonances (LSPR) at visible wavelengths.<sup>8–10</sup> The LSPR phenomenon consists of the coherent and collective oscillations of conduction band electrons at NP–dielectric interfaces (surface plasmons) excited by incident photons. Surface plasmons dephase in 3–30 fs through either radiative damping (which results in re-emission of the photon) or through non-radiative damping processes such as surface scattering, Landau (intradband) damping, interband damping, and chemical interface damping, which result in the creation of hot-carrier pairs.<sup>11,12</sup> The statistics of the geminate electrons and holes formed by plasmon decay follow a Fermi–Dirac distribution corresponding to a large effective electron temperature compared to room temperature due to which these carriers are said to be “hot.”<sup>12</sup> Furthermore, the energies of the geminate hot carriers are not necessarily evenly distributed. In gold NPs, the hot holes have higher effective temperatures than the hot electrons.<sup>13</sup> The key goal in carrier-driven plasmonic catalysis is to utilize the excess energy of hot carriers to drive a chemical reaction before they are lost to thermal relaxation or electron–hole recombination.

The utilization of hot carriers in plasmonic catalysts presents a particular challenge due to the ultrafast nature of relaxation processes and the poor catalytic activity of plasmonic noble metal surfaces.<sup>3,14</sup> Hot carriers lose energy by electron–electron collisions in <100 fs and experience phonon scattering in ~1 ps.<sup>15</sup> A number of research reports have shown that hot electrons in Au can be injected across a Schottky barrier formed in a heterojunction with a catalytically active, wide band gap n-type semiconductor, before the thermal equilibration.<sup>5,16</sup> Such hot electron heterojunction photocatalysts have been used to perform CO<sub>2</sub> photoreduction, nitrobenzenethiol photoreduction, oxidative dye degradation, photoreduction of

bicarbonate, and so forth.<sup>17–22</sup> On the other hand, there are very few reports on the harvesting of hot holes in plasmonic catalysts. Even rarer are reports on high-performance photo-voltaic or photoelectrochemical (PEC) devices that rely on the extraction of hot holes from Au NPs. A fundamental problem is that Schottky barriers, across which hot holes can be injected, are typically formed between p-type semiconductors and low work-function metals. Since gold is a high work-function metal, it tends to form Ohmic contacts with p-type semiconductors and renders it rather difficult to construct hot hole-harvesting Schottky junctions. Recent attempts at using organic hole transport layers to extract hot holes from Au NPs reported photocurrent densities <100  $\mu\text{A cm}^{-2}$  under solar illumination.<sup>23</sup> We present an unorthodox solution to the aforementioned problem of hot hole extraction from Au NPs. Our approach makes use of amorphous TiO<sub>2</sub> (a-TiO<sub>2</sub>) as a hole collection layer and is successful in generating photocurrents approaching 4 mA cm<sup>-2</sup> in the methanol-containing KOH electrolyte under AM1.5G 1 sun illumination.

## 2. RESULTS AND DISCUSSION

### 2.1. Structure, Composition, and Optical Properties of Au@a-TiO<sub>2</sub> Photoanodes.

We formed a single layer of hemispherical gold nanoislands (~50 nm average diameter) on fluorine-doped tin oxide (FTO)-coated glass substrates by vacuum deposition followed by spontaneous thermal dewetting. The He ion micrograph in Figure 1a, provides evidence that annealing at 550 °C was successful in dewetting the sputtered gold film. The morphology and size distribution of the Au nanoislands are shown in Figure S2a in Supporting Information. The Au NPs were coated with a ~10 nm layer of a-TiO<sub>2</sub> using atomic layer deposition (ALD). The clear distinction between the Au (core) and TiO<sub>2</sub> (shell) in the core–shell structure of the fabricated photoelectrode is clearly

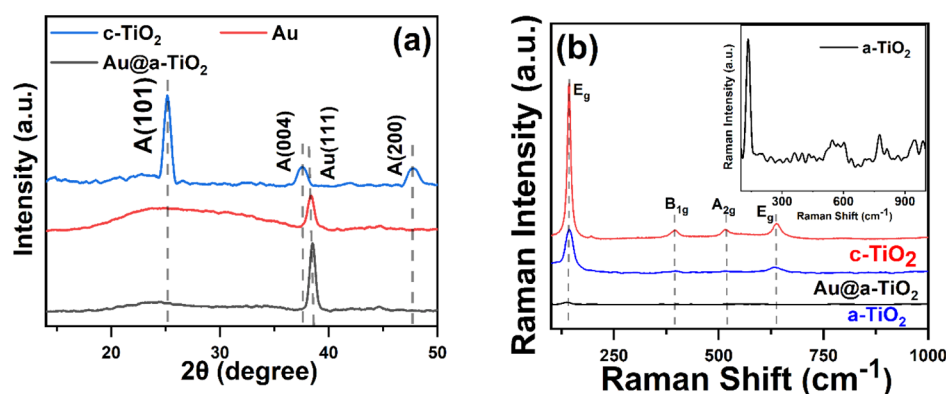


**Figure 2.** (a) XRD patterns of gold, c-TiO<sub>2</sub>, and Au@a-TiO<sub>2</sub>. The Au@a-TiO<sub>2</sub> core-shell NPs. A denotes the peaks corresponding to anatase TiO<sub>2</sub>. (b) Raman spectra of a-TiO<sub>2</sub>, Au@a-TiO<sub>2</sub>, and c-TiO<sub>2</sub>. The substrate was FTO-coated glass in each case.

shown in the helium ion images of Au@a-TiO<sub>2</sub> (Figure 1b). Following the dewetting, the surface of FTO was exposed in the inter-nanoisland gaps. Since ALD is a cyclic, conformal, and precise deposition process, the deposition of a-TiO<sub>2</sub> on the hemispherical Au nanoislands formed a shell around the gold core and also completely covered the exposed surface of FTO in the Au@a-TiO<sub>2</sub> sample (Figure S2b).

The UV-vis spectrum of the Au sample (indicated by a solid black line) exhibits a peak at around 560 nm (Figure 1c), which is the characteristic LSPR peak of 50 nm Au NPs bounded by air and FTO/glass, which is accurately reproduced by the finite difference time domain (FDTD) electromagnetic simulation result (red curve in Figure 1d). It is well known that the plasmon resonance is exquisitely sensitive to the permittivity of the medium surrounding the metal. The LSPR peak of Au shifted from 560 to 650 nm after deposition of the a-TiO<sub>2</sub> shell (red curve in Figure 1c) which is attributable to the much higher refractive index of a-TiO<sub>2</sub> compared to air, thus shifting the Fröhlich resonance condition to longer wavelengths. The dramatic red-shift of the LSPR to 650 nm is also captured by the FDTD-simulated absorption cross-section of the Au@a-TiO<sub>2</sub> sample (blue curve in Figure 1d). The FDTD simulations were performed for isolated Au NPs and ignored the effect of polydispersity-induced inhomogeneous broadening present in real samples. Consequently, the FDTD-simulated spectra in Figure 1d show narrower peaks than the measured spectra in Figure 1c. The sharp rise in absorption for wavelengths below 350 nm in the measured spectra (Figure 1c) is due to the absorption edge of the FTO substrate, which is a degenerately doped semiconductor. The 10 nm TiO<sub>2</sub> coating contributes very little to the observed absorption. The FDTD-simulated cross-section of the electric field distribution for a single Au@a-TiO<sub>2</sub> particle excited at resonance (650 nm) demonstrates a strong local field enhancement at the interface between the Au NPs and the a-TiO<sub>2</sub> shell. These are indicated by the intense red spots in Figure 1e where a nearly sixfold enhancement of the local field is seen. In addition, a portion of the radiated light intensity, which would otherwise have been scattered in air, propagates through the FTO-coated glass substrate, as evidenced by the concentric rings of decreasing field strength behind the Au NP in Figure 1e. This is due to the much higher refractive index of FTO (~1.85) compared to air.

The X-ray diffraction (XRD) patterns of Au (green line in Figure 2a) and Au@a-TiO<sub>2</sub> (red line in Figure 2a) samples reveal the presence of the face-centered cubic metallic Au

(111) reflection at a  $2\theta$  value of 39° (JCPDS# 04-784). No peaks related to anatase or rutile or brookite TiO<sub>2</sub> were detected, suggesting that the ALD-deposited TiO<sub>2</sub> is primarily amorphous and lacks long-range order. An ALD-deposited TiO<sub>2</sub> on a glass substrate sample was annealed at 450 °C for 2 h to verify the induction of crystallinity with elevated temperature processing. The XRD pattern of the annealed ALD TiO<sub>2</sub> sample (c-TiO<sub>2</sub>—blue line in Figure 2a) corresponding to JCPDS# 21-1272 shows all the peaks corresponding to the anatase phase, thus proving that the annealing does indeed change the structure of the ALD TiO<sub>2</sub> from amorphous to crystalline. Another powerful tool for investigating the ordered-disordered TiO<sub>2</sub> structures is Raman spectroscopy.<sup>24</sup> The Raman spectra of the a-TiO<sub>2</sub>, c-TiO<sub>2</sub>, and Au@a-TiO<sub>2</sub> samples are shown in Figure 2b. Due to the absence of long-range order, the characteristic phonon modes of anatase are extremely weak in a-TiO<sub>2</sub> (black curve in Figure 2b). The c-TiO<sub>2</sub> sample (blue curve in Figure 2b) exhibited an intense peak at *ca.* 145 cm<sup>-1</sup>, which belongs to the E<sub>g</sub> mode with three less intense peaks at 395, 516, and 640 cm<sup>-1</sup>, which belong to B<sub>1g</sub>, A<sub>2g</sub>, and E<sub>g</sub> modes, respectively. Compared to the annealed sample, the Au@a-TiO<sub>2</sub> (red curve in Figure 2b) exhibited less intense peaks at the same wavenumbers, which indicates that a-TiO<sub>2</sub> is disordered and may possess some short-range order at best.<sup>25</sup> The chemical composition and corresponding binding energies of the Au@a-TiO<sub>2</sub> sample were investigated by X-ray photoelectron spectroscopy (XPS). The XPS elemental survey scan shows the presence of Ti 2p, Ti 2s, O 1s, Au 4f, and Au 4d peaks (Figure S3a), which provides evidence of all the elements of Au and TiO<sub>2</sub>. Deconvoluted peaks of the high-resolution XPS scan in the O 1s region exhibit three peaks centered at 530.2, 531.1, and 532.4 eV. These peaks correspond to Ti-O, oxygen vacancies (V<sub>O</sub>), and surface chemisorbed oxygen (C<sub>O</sub>), respectively.<sup>26-28</sup> Similarly, the decomposition of the peaks at the Ti 2p region exhibits two major peaks centered around 459 and 465 eV, which can be attributed to Ti 2p<sub>3/2</sub> and Ti 2p<sub>1/2</sub> of Ti<sup>4+</sup> in the TiO<sub>2</sub> crystal structure, respectively.<sup>29,30</sup> The presence of gold in the Au@a-TiO<sub>2</sub> sample was confirmed using two deconvoluted peaks at 84 and 87.6 eV, which were assigned to Au 4f<sub>7/2</sub> and Au 4f<sub>5/2</sub>, respectively.<sup>31</sup> Figure S3e depicts the XPS depth profile of elements of interest (Ti, Au, and Sn) of the Au@a-TiO<sub>2</sub> photoelectrode to track the presence of a-TiO<sub>2</sub>, Au, and SnO<sub>2</sub>, respectively, as a function of etch depth. For the depth profile scan, the Ti 2p<sub>3/2</sub> peak was used to track the abundance of a-TiO<sub>2</sub>, Au 4f<sub>5/2</sub> to track the

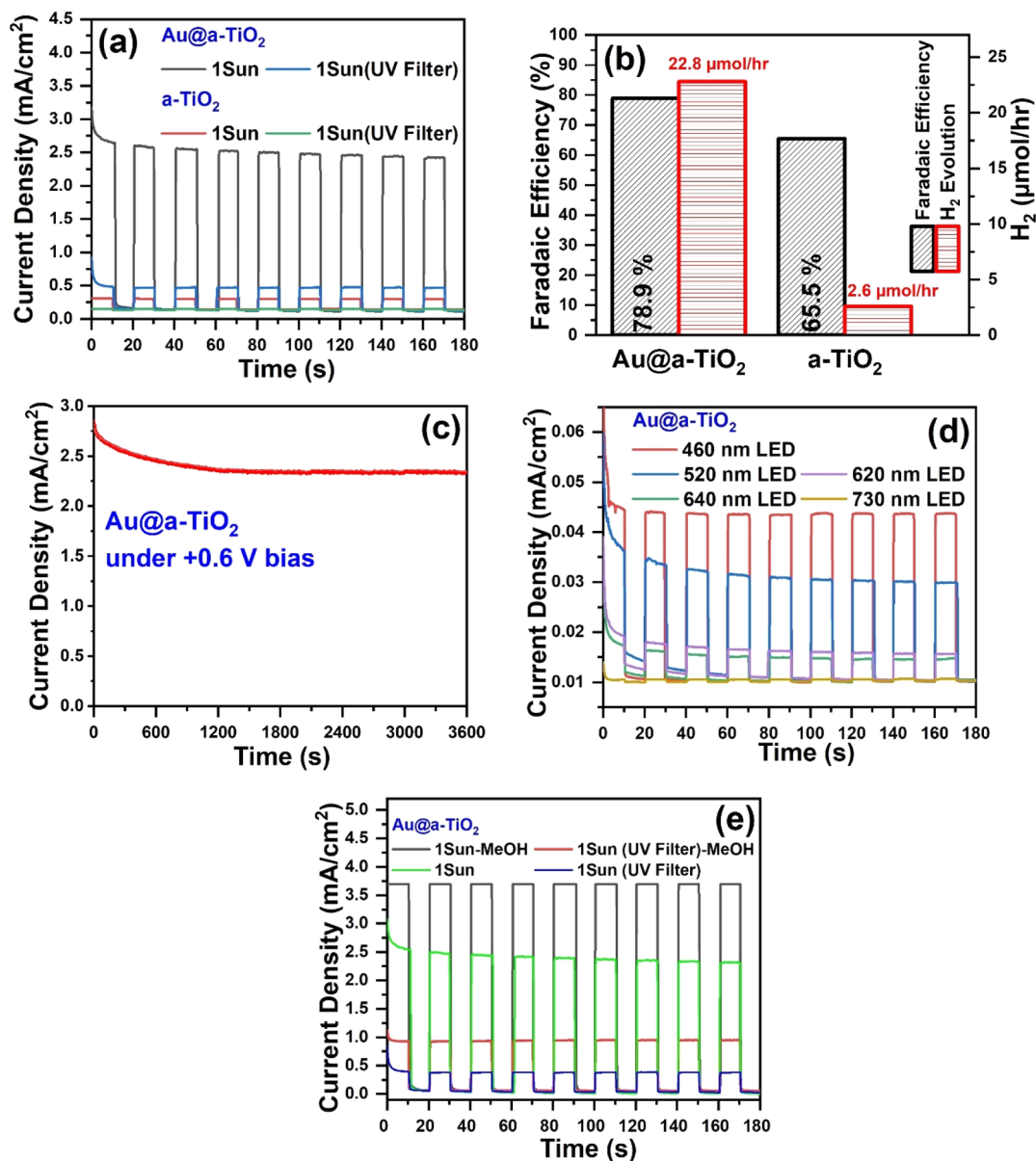


**Figure 3.** (a) PEC measured  $i-t$  curves of Au@a-TiO<sub>2</sub> and a-TiO<sub>2</sub> using the solar simulator and solar simulator with UV cutoff illumination under +0.6 V applied potential vs Ag/AgCl reference electrode in a 1 M KOH electrolyte with on/off switch. (b) Corresponding H<sub>2</sub> evolution and Faradaic efficiency of Au@a-TiO<sub>2</sub> under solar simulator illumination. (c) Long duration PEC measured  $i-t$  curves of Au@a-TiO<sub>2</sub> using the solar simulator under +0.6 V applied potential vs Ag/AgCl reference electrode in a 1 M KOH electrolyte without on/off switch. (d) PEC measured  $i-t$  curves of Au@a-TiO<sub>2</sub> using visible LED illumination under +0.6 V applied potential vs Ag/AgCl reference electrode in a 1 M KOH electrolyte. (e) Comparison between the PEC measured  $i-t$  curves of Au@a-TiO<sub>2</sub> using the solar simulator and solar simulator with UV cutoff illumination under +0.6 V applied potential vs Ag/AgCl reference electrode in a 1 M KOH electrolyte with and without hole scavengers (MeOH).

abundance of Au, and Sn 3d to track the presence of FTO. The core@shell architecture of the Au@a-TiO<sub>2</sub> heterojunction is evidenced by this depth profile scan in which the outer surface is completely covered with ALD-deposited a-TiO<sub>2</sub>. As the sputter etching continues, the abundance of the Au increases. The depth profile also confirms that the ALD deposition of a-TiO<sub>2</sub> layer was successful in covering the area of the FTO surface, which was exposed after annealing (dewetting) of the sputtered Au film as Ti could be found even near the surface of FTO (shown by the abundance of the Sn in the XPS depth profile). In the Au@a-TiO<sub>2</sub> core-shell photoanodes, the Au NPs are never in direct contact with the electrolyte. In this case, the Au core solely acts as an optical antenna and does not directly oxidize or reduce hydroxyl ions or protons in the

water-splitting reaction.<sup>32</sup> As a result, the amorphous ALD-deposited TiO<sub>2</sub> plays the dual role of a charge carrier acceptor and protective layer.<sup>33</sup>

## 2.2. PEC Performance of the Au@a-TiO<sub>2</sub> Photoanode.

The ultrathin Au@a-TiO<sub>2</sub> core-shell NP photoanode proved itself to be an excellent photoanode for the sunlight-driven splitting of water (Figure 3). As previously shown (in Figure 1c) and discussed, the Au@a-TiO<sub>2</sub> photoelectrode exhibits appreciable light absorption in the visible light region, that is, photons of wavelength >420 nm. The photocurrent response of Au@a-TiO<sub>2</sub> in comparison with the a-TiO<sub>2</sub> layer was investigated using linear sweep voltammetry (LSV) under AM1.5G 1 sun excitation and ultraviolet-filtered visible light (i.e., AM1.5G 1 sun illumination with a 420 nm long pass

filter). Under AM1.5G 1 sun illumination, Au@a-TiO<sub>2</sub> revealed a remarkable photoresponse of 2.5 mA cm<sup>-2</sup>, while the photoresponse of a-TiO<sub>2</sub> was only 0.3 mA cm<sup>-2</sup>. The PEC performance of the Au@a-TiO<sub>2</sub> core-shell photoanode is impressive in both relative and absolute terms. Even several micrometer thick films of traditional n-type semiconductor photoanodes made of TiO<sub>2</sub>, anion-doped TiO<sub>2</sub>, SrTiO<sub>3</sub>, WO<sub>3</sub>, and g-C<sub>3</sub>N<sub>4</sub>/TiO<sub>2</sub> have only been able to generate 1–2 mA cm<sup>-2</sup> of photocurrent under AM1.5G 1 sun illumination.<sup>34,35</sup> Therefore, the ability of the Au@a-TiO<sub>2</sub> to not merely match but exceed this performance is impressive, and doubly impressive when the ultrathin nature of the photoanode (<100 nm in thickness) is taken into account. Under both 1 sun and UV-filtered 1 sun illumination, the photoresponse of Au@a-TiO<sub>2</sub> is almost 8.3 and 5 times that of the a-TiO<sub>2</sub> photoelectrode under identical conditions, conclusively demonstrating the dominant role of Au and plasmonic hot carriers in the water oxidation process. These results can be understood by recognizing that interband damping is a dominant plasmon dephasing mechanism for Au NPs sized 25–75 nm used in this work (Figure S2a), contributing more than half of the observed homogeneous line width broadening.<sup>36</sup> Consider the behavior of hot-carrier pairs formed by interband damping of the Au surface plasmon excited by high-energy ( $\lambda < 420$  nm) photons. Ultrafast transfer of hot electrons from Au NPs to indium tin oxide (ITO)-coated glass substrates is known,<sup>37</sup> and there is every reason to expect comparable or faster hot e-transfer from Au@a-TiO<sub>2</sub> core-shell NPs to the FTO substrate in this work, considering the similar electronic properties of ITO and FTO and the higher roughness of FTO compared to ITO (enhanced local *E*-fields and more numerous hot spots). Hot holes in Au are transferred to trap levels of a-TiO<sub>2</sub> where a nonthermal distribution of carriers is maintained, resulting in the reduction of thermalization losses.<sup>38</sup> The thin a-TiO<sub>2</sub> shell is electron rich under AM1.5G 1 sun illumination due to excitation by UV photons and the simultaneous inability to transfer electrons to protons at the surface (the TiO<sub>2</sub> surface is deprotonated in 1 M KOH). Consequently, the already electron-rich a-TiO<sub>2</sub> shell is unable to accept further hot electrons from Au, which accounts for the seemingly unidirectional flow of hot holes from Au into TiO<sub>2</sub> under AM1.5G 1 sun illumination. We measured the hydrogen resulting from water splitting using a H cell (experimental details in the Supporting Information), and the results are shown in Figure 3b. Under 1 sun illumination, the Au@a-TiO<sub>2</sub> exhibits a remarkable H<sub>2</sub> production rate of 22.8  $\mu\text{mol h}^{-1}$  (corresponding to a faradaic efficiency of ~79%) which is almost 10 times larger than the H<sub>2</sub> production rate of the a-TiO<sub>2</sub> photoelectrode (2.6  $\mu\text{mol h}^{-1}$ ). The relatively high faradaic efficiency of both a-TiO<sub>2</sub> and Au@a-TiO<sub>2</sub> photoanodes indicates the absence of major side reactions. Dominant fractions of the generated photocurrents are consumed in PEC water splitting.

The stability of the photoelectrode is an important factor for PEC water-splitting applications. The variation of the photocurrent as a function of time (*i*-*t* curve) can be used as a figure of merit for photoelectrode's stability.<sup>39</sup> The *i*-*t* curves with on/off switch of the Au@a-TiO<sub>2</sub> and a-TiO<sub>2</sub> photoelectrodes at an applied bias of +0.6 V versus the Ag/AgCl counter electrode are shown in Figure 3a. Since the Au@a-TiO<sub>2</sub> exhibited the best photoresponse among the fabricated the samples, its long run stability test was conducted. Figure 3c exhibits the photoresponse of the Au@a-TiO<sub>2</sub> photoanode

under an applied bias of +0.6 V in the KOH electrolyte under 1 h illumination without on/off switching. As it is evident by this measurement, it is seen that the Au@a-TiO<sub>2</sub> samples exhibited a stable photoresponse during 1 h irradiation which confirms that the Au@a-TiO<sub>2</sub> can sustain the PEC water-splitting reaction for long period of time.

**2.3. Processes Underlying the PEC Performance of Au@a-TiO<sub>2</sub> Photoanodes.** Figure S4a shows that the dark current was small (<0.45 mA cm<sup>-2</sup>) for Au@a-TiO<sub>2</sub> and negligibly small (<0.02 mA cm<sup>-2</sup>) for a-TiO<sub>2</sub>. TiO<sub>2</sub> has a large concentration of trapped holes at the surface which are subject to nucleophilic attack by water molecules. The onset potential for the flow of positive anodic current through the a-TiO<sub>2</sub> electrode was -0.88 V versus Ag/AgCl in the dark and shifted to -0.98 V versus Ag/AgCl under AM1.5G 1 sun illumination, which is consistent with prior reports on TiO<sub>2</sub>-based photoanodes in highly basic electrolytes. The magnitude of the anodic current is limited by the poor hole mobility of disordered a-TiO<sub>2</sub> which limits replenishment of the holes captured by water molecules. On the other hand, the onset potential for Au@a-TiO<sub>2</sub> is -0.49 V versus Ag/AgCl in the dark and shifts to -0.72 eV under AM1.5G 1 sun illumination, and the corresponding anodic currents are larger by an order of magnitude. This indicates the number of trapped holes to be smaller on the surface of Au@a-TiO<sub>2</sub> likely due to charge transfer from TiO<sub>2</sub> to Au during the junction formation and equilibration. The injection of holes from Au into disordered TiO<sub>2</sub> under positive anodic bias causes trap filling and a higher effective hole mobility in the a-TiO<sub>2</sub> shell around the Au, resulting in larger anodic currents in both the dark and under 1 sun illumination. One interesting observation is the significant decrease in the magnitude of the photovoltage and anodic photocurrent of Au@a-TiO<sub>2</sub> samples when UV-filtered visible light is incident. The onset potential and anodic current density (at +0.6 V) bias are -0.25 V versus Ag/AgCl and 0.47 mA cm<sup>-2</sup>, respectively. We attribute this decrease to the bidirectionality of charge flow during visible light illumination. a-TiO<sub>2</sub> is not excited by visible light illumination and therefore does not possess excess electrons. Hot electrons generated by intraband damping of Au plasmons are injected into both the a-TiO<sub>2</sub> shell and FTO substrate. Hot holes are still injected from Au into a-TiO<sub>2</sub> albeit fewer in number than that for UV excitation due to weaker interband damping of plasmons excited by lower energy photons. This is because the minimum threshold energy for interband damping in Au is 2.3 eV, and the probability of interband transitions sharply decreases below ~2.4 eV.<sup>40</sup> The hot electrons and hot holes injected into a-TiO<sub>2</sub> recombine causing a reduction in both the anodic photovoltage and photocurrent density under UV-filtered solar illumination. However, the photocurrent density remains positive (anodic), indicating that the number of holes injected from Au into a-TiO<sub>2</sub> still exceeds the number of injected electrons. This type of wavelength-dependent directionality and magnitude of carrier flow in Au-TiO<sub>2</sub> heterojunctions have been previously reported in the context of CO<sub>2</sub> photoreduction<sup>18</sup> but is novel in the context of PEC water splitting.

Investigation of the visible light photocurrent generation of the Au@a-TiO<sub>2</sub> sample was conducted using a set of light-emitting diodes (LEDs) with emission centered at 460, 520, 620, 640, and 730 nm, each with a bandwidth of 10 nm. The LSV and *i*-*t* curves using this set of LEDs are shown in Figures S4b and 3d, respectively. The photocurrent was anodic under

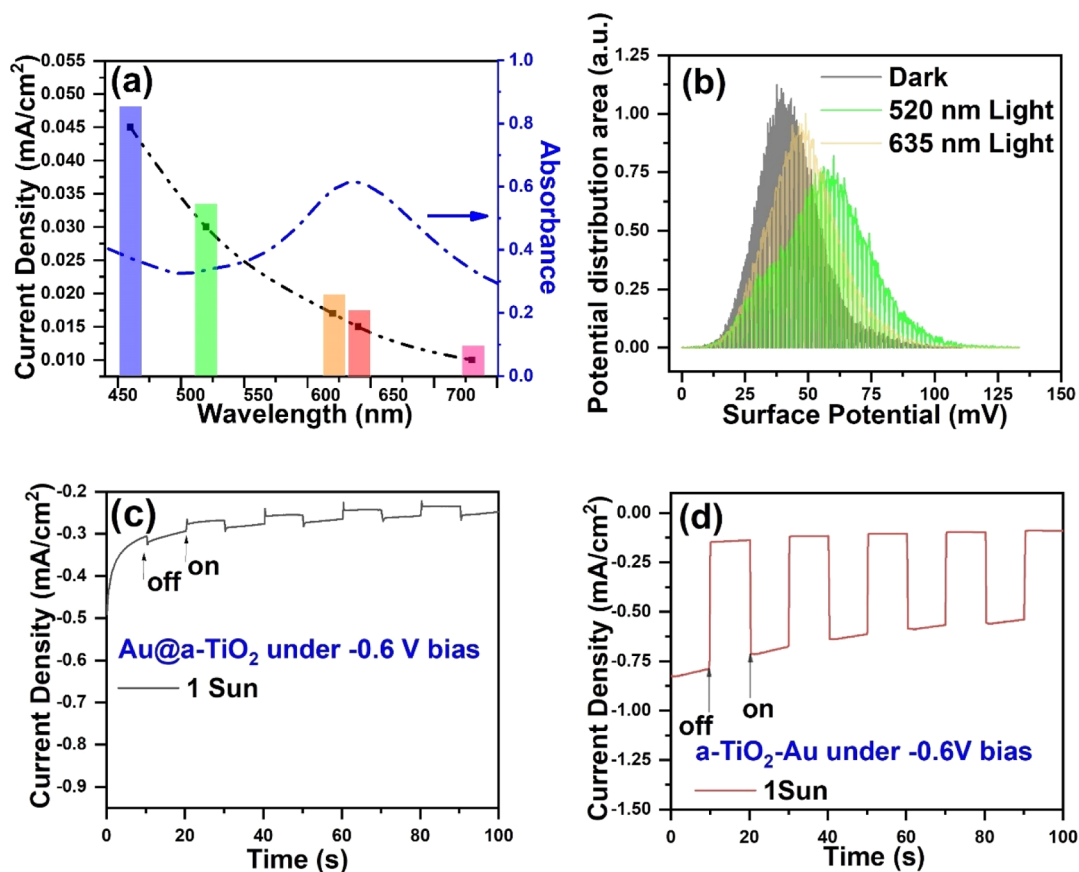


**Figure 4.** (a) Corresponding action spectrum of Au@a-TiO<sub>2</sub> under LED illumination. (b) Surface potential of the Au@a-TiO<sub>2</sub> photoelectrode under 520 nm and 635 nm excitations. (c) Measured *i*-*t* curves of Au@a-TiO<sub>2</sub> using the solar simulator under -0.6 V applied potential vs Ag/AgCl reference electrode in a 1 M Na<sub>2</sub>SO<sub>4</sub> electrolyte. (d) Measured *i*-*t* curves of a-TiO<sub>2</sub>-Au using the solar simulator under -0.6 V applied potential vs Ag/AgCl reference electrode in a 1 M Na<sub>2</sub>SO<sub>4</sub> electrolyte.

the excitation of each of these LEDs. Au@a-TiO<sub>2</sub> showed the highest photoresponse under 460 nm excitation. The photoresponse gradually decreased with increasing wavelength. Another figure of merit for evaluation of plasmon-induced PEC water splitting is the photocurrent measurement as a function of the excitation wavelength, also known as the action spectrum.<sup>41,42</sup> Figure 4a depicts the corresponding visible light action spectrum of the Au@a-TiO<sub>2</sub> photoanode using the *i*-*t* curves (the absorption spectrum of Au@a-TiO<sub>2</sub> in the visible light region is also shown by a dotted blue line to guide the eyes). The action spectra of the Au@a-TiO<sub>2</sub> photoanode did not follow the LSPR peak and showed a gradual decrease as the wavelength increased. This is characteristic of plasmonic photocatalysts where interband damping of the plasmon is the dominant source of hot-carrier generation. When intraband damping is the primary generator of hot carriers, the action spectrum has the same profile as the LSPR optical extinction spectrum. To further elucidate the charge-transfer phenomena in the Au@a-TiO<sub>2</sub> photoanode, we utilized scanning Kelvin probe force microscopy (KPFM) to measure the surface potential of the samples.<sup>43,44</sup> To analyze the viability of the injection of hot holes from Au into the outer a-TiO<sub>2</sub> shell, the surface potential of Au@a-TiO<sub>2</sub> photoelectrode was measured using KPFM under two illumination sources of 520 and 635 nm. The results are shown in Figure 4b. Since the a-TiO<sub>2</sub> shell is the outer layer in Au@a-TiO<sub>2</sub> sample, the KPFM result is the representation of the potential of the shell (a-TiO<sub>2</sub>). According to Figure 4b, when Au@a-TiO<sub>2</sub> is subjected to 635

and 520 nm excitations, the surface potential is shifted to positive side in each case compared to the dark condition. Interestingly, the 520 nm excitation resulted in a more positive surface potential compared to 635 nm illumination of identical power and the dark, which is in good agreement with the action spectrum graph in which the photocurrent generation was higher for excitation by higher energy photons, further confirming the role of interband damping and hot hole extraction by TiO<sub>2</sub>. Methanol, a known hole scavenger, was used in the electrolyte (see the materials and methods section in the Supporting Information) to quickly react with photogenerated holes in Au@a-TiO<sub>2</sub> before they recombine.<sup>45</sup> Figure 3e shows the *i*-*t* curves of the Au@a-TiO<sub>2</sub> photoanode using methanol as the hole scavenger. A large photocurrent enhancement effect was seen when methanol was used in the electrolyte as a hole scavenger under photoexcitation by 1 sun and visible light (using the UV cutoff filter). This further proves that the fabricated Au@a-TiO<sub>2</sub> photoelectrode supplies photogenerated holes to the electrolyte during the water-splitting reaction. The principal mechanism for the increase in photocurrent density for the Au@a-TiO<sub>2</sub> photoanode from 2.5 to 3.7 mA cm<sup>-2</sup> upon methanol addition to the electrolyte is the current doubling effect.<sup>46</sup> The current doubling effect occurs due to the methanol molecules accepting a hole from the valence band of a n-type semiconductor photoanode and then also injecting electrons into the conduction band of the photoanode.<sup>47</sup> While the adsorbed water and hydroxyl ions are known to react with mobile holes, methanol is also capable of

reacting with immobile trapped holes in  $\text{TiO}_2$ .<sup>48,49</sup> Therefore, the increase in photocurrent density at anodic bias of 0.6 V under AM1.5G 1 sun illumination due to the addition of methanol from 2.5 to 3.7  $\text{mA cm}^{-2}$  (Figure 3e) is due to the current doubling effect and more efficient extraction of holes from the surface of  $\text{Au@a-TiO}_2$ .

Two sets of complementary experiments were conducted to study the charge-transfer mechanism in the  $\text{Au@a-TiO}_2$  photoelectrodes. First, instead of using the  $\text{Au@a-TiO}_2$  as a photoanode (applying positive +0.6 V bias to the photoelectrode), this heterostructure was used as a photocathode by applying a negative bias to it (−0.6 V). Figure 4c exhibits the AM1.5 1 sun photocurrent repose of this photoelectrode under negative bias in a 1 M  $\text{Na}_2\text{SO}_4$  electrolyte. Interestingly, the results show a weak anodic photocurrent which means that even under applied negative bias to the  $\text{Au@a-TiO}_2$  photoelectrode, Au NPs are still injecting the holes to the outer  $\text{a-TiO}_2$  shell. This indicates an unusually strong driving force. Second, the architecture of the  $\text{Au@a-TiO}_2$  was reversed by changing the sequence of deposition of  $\text{a-TiO}_2$  and Au (the thin layer of  $\text{a-TiO}_2$  was deposited on the FTO substrate at first, and then, the Au films were sputtered on top of it). This photoelectrode was named as  $\text{a-TiO}_2\text{-Au}$  photoelectrode. In this case, the Au NPs are only in direct contact with the thin  $\text{a-TiO}_2$  layer and not with the FTO. Interestingly, when the applied voltage was −0.6 V against the reference electrode, the  $\text{a-TiO}_2\text{-Au}$  photoelectrode exhibited cathodic photocurrent (Figure 4d), which indicates the injection of holes into the  $\text{a-TiO}_2$  layer and driving the reduction reaction at the interface of the  $\text{a-TiO}_2\text{-Au}$  and the electrolyte; these results again confirm the possibility of the injection of holes into the thin  $\text{a-TiO}_2$  layer. The corresponding results for a 1 M KOH electrolyte are similar and shown in Figure S5 in Supporting Information. Overall, the action spectrum measurement, hole scavenger tests, along with KPFM, near-infrared (NIR) UV-vis spectra, and changing the architecture of the  $\text{Au@a-TiO}_2$  photoelectrode are well aligned with each other and suggest the injection of hot holes into the outer  $\text{a-TiO}_2$  shell. These results not only confirm earlier work which indicates Au NPs embedded in  $\text{TiO}_2$ <sup>50–52</sup> to exhibit higher local field enhancements and function as superior photoanodes compared to Au NP-decorated  $\text{TiO}_2$  films for water oxidation but also go beyond to show that the directionality of charge transfer is very important. Figure S6 in Supporting Information shows that the  $\text{a-TiO}_2\text{-Au-a-TiO}_2$  photoanode underperforms the  $\text{Au@a-TiO}_2$  photoanode for PEC water splitting. This is because a direct connection between Au and FTO is important to ensure that plasmonic electrons from Au are injected into FTO, while hot holes are injected from Au into  $\text{TiO}_2$ . The  $\text{a-TiO}_2\text{-Au-a-TiO}_2$  configuration lacks this direct connection between Au and FTO. When both electrons and holes are injected from Au into  $\text{TiO}_2$  and present at very high densities in an ultrathin  $\text{TiO}_2$  film, fast Auger recombination will dominate.<sup>53</sup>

The Mott–Schottky plot for  $\text{a-TiO}_2$  (Figure S7c in Supporting Information) exhibits the typical positive slope of an n-type semiconductor. The carrier concentration for  $\text{a-TiO}_2$  was estimated to be  $10^{20}$  to  $10^{21} \text{ cm}^{-3}$ , which is relatively high, and further supports the presence of oxygen vacancies in  $\text{a-TiO}_2$  indicated by the XPS data. While 10 nm thick films are usually unable to support band-bending due to insufficient charge available to be depleted, the high self-doping of  $\text{a-TiO}_2$  film renders it capable of forming a depletion region. The Mott–Schottky plot of  $\text{Au@a-TiO}_2$  showed an increase in the

positive slope which corresponds to a lower carrier concentration and the formation of a wider depletion region with an estimated 3–10 nm width. The ultraviolet photoelectron spectra (UPS) of Au,  $\text{a-TiO}_2$ , and  $\text{Au@a-TiO}_2$  are shown in Figure S7a in Supporting Information. The work function ( $\phi_s$ ) of Au,  $\text{a-TiO}_2$ , and  $\text{Au@a-TiO}_2$  photoelectrodes were calculated to be 4.61, 3.5, and 3.81 eV, respectively, using the expression  $\phi_s = h\nu - E_{\text{SE}}$  in which  $h\nu$  is the energy of the photons used to investigate the band structure (21.21 eV) and  $E_{\text{SE}}$  is the secondary electron cutoff energy.<sup>54</sup> The low work function of  $\text{a-TiO}_2$  is a result of strong n-type behavior and band gap widening. The band gap of very thin, amorphous ALD-grown  $\text{TiO}_2$  films has been reported to be as high as 4.5 eV due to a combination of carrier localization and quantum confinement effects.<sup>55–57</sup> UPS is an extremely surface-sensitive technique with a depth resolution of a few monolayers (~1–2 nm). Gold is not exposed at the surface of  $\text{Au@a-TiO}_2$  samples. Therefore, the work function measured for  $\text{Au@a-TiO}_2$  is that of the  $\text{a-TiO}_2$  shell covering the gold. The measured work function of 3.81 eV for  $\text{Au@a-TiO}_2$  indicates a deeper Fermi level in  $\text{a-TiO}_2$  due to depletion of electrons and the formation of a Schottky junction with Au. The valence band maxima of  $\text{a-TiO}_2$  and  $\text{Au@a-TiO}_2$  are located 4.00 and 3.27 eV, respectively, below the Fermi level (Figure S7b in Supporting Information). The decrease in the valence band maximum for the  $\text{Au@a-TiO}_2$  photoelectrode compared to  $\text{a-TiO}_2$  indicates upward band-bending at the  $\text{Au-a-TiO}_2$  interface and confirms the formation of a Schottky junction.<sup>54</sup>

Excess carriers in amorphous or partially crystalline  $\text{TiO}_2$  can have unusually long lifetimes extending to several hours due to the high dielectric relaxation time and the low probability of direct recombination of trapped holes with trapped electrons, which manifests itself in persistent photoconductivity (PPC).<sup>56,58</sup> The practical implication of PPC for plasmonic photocatalysis is that once hot carriers are injected from Au into the thin  $\text{a-TiO}_2$  shell and subsequently captured by deep traps in  $\text{TiO}_2$ , the resulting carrier distribution is nonthermal and can remain that way for relatively long durations (minutes to hours). This enables hot holes injected from Au into  $\text{TiO}_2$  to remain hot and results in the reduction of thermalization losses together with a concomitant increase in photovoltage and thermodynamic driving force for water oxidation.<sup>38</sup> Prior reports indicate that long-lived excess carriers in  $\text{TiO}_2$  injected from gold can be detected through the increased NIR absorption of free carriers.<sup>18</sup> To investigate whether such long-lived excess carriers are also present in  $\text{Au@a-TiO}_2$ , the UV-vis spectra of the  $\text{Au@a-TiO}_2$  from ultraviolet to the NIR region were recorded before and after 1 h of visible light illumination (Figure S7d). The illumination with visible light excites the LSPR of Au NPs, and subsequent plasmon decay is followed by hot electron injection into both FTO and  $\text{TiO}_2$  and hole injection into  $\text{TiO}_2$ . On a net basis,  $\text{TiO}_2$  receives an excess of holes and FTO receives an excess of electrons, as indicated by the previously discussed KPFM data. A large percentage of the injected carriers of both polarities will likely be captured by deep level traps in  $\text{TiO}_2$ , and the resulting trap filling will also increase the overall concentration of mobile carriers. Indeed, Figure S7d shows an increase in the NIR absorption due to a larger population of mobile carriers. The inset of Figure S7d exhibits the difference between the LSPR peak-normalized UV-vis spectra of  $\text{Au@a-TiO}_2$  before and after visible light illumination. Interestingly, the normalized difference spectra show a dip around 1750 nm which is

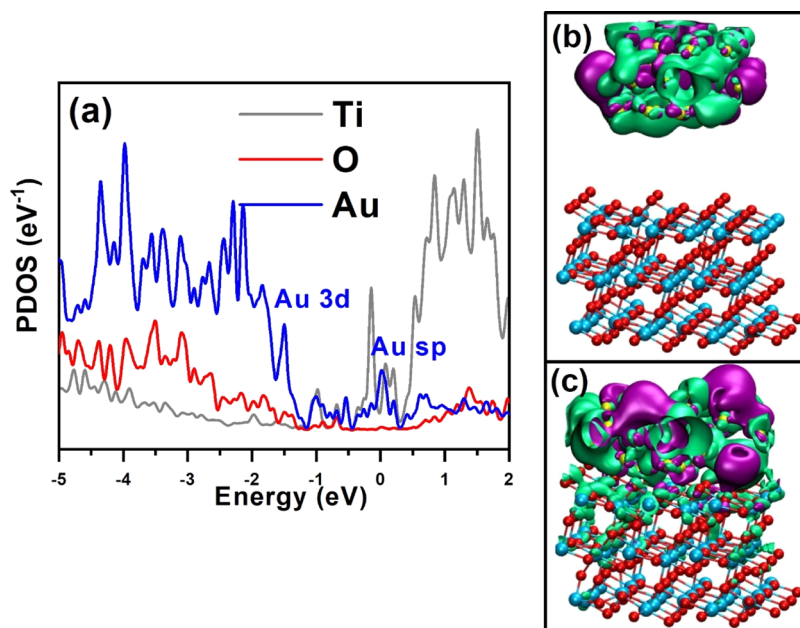


**Figure 5.** (a) PDOS of selected atoms for Au@a-TiO<sub>2</sub> heterostructures. Oxygen-vacant perturbed anatase TiO<sub>2</sub> (101) and Au (111) were chosen for DFT modeling. The DFT-optimized structure showing the HOMO and LUMO of Au@a-TiO<sub>2</sub> heterostructures in (b) close and (c) far configuration. Purple and green colors are for HOMO and LUMO surfaces, respectively. Ti, O, and Au atoms are shown in light blue, red, and yellow colors, respectively.

probably due to an excess carrier-mediated shift in the plasmon resonance of FTO which is known to occur between 1500 and 2100 nm.<sup>59,60</sup>

When the size of the plasmonic NP is <100 nm in an LSPR excited plasmonic metal/semiconductor heterojunction, there are two possible ways that the charge can transfer between the excited plasmon and the semiconductor: the first way is the plasmon resonance energy transfer (PRET) occurring over longer ranges, and the second one is short-range hot-carrier injection.<sup>41,61,62</sup> We have made a strong case in this work for interband damping-mediated hot hole injection from Au into TiO<sub>2</sub> under AM1.5G 1 sun illumination. Now, we will rule out the possibility of PRET occurring in Au@a-TiO<sub>2</sub>. In PRET, the plasmon energy directly transfers to the nearby semiconductor and creates electron–hole pairs in the conduction and valence bands of the semiconductor, respectively. The main prerequisite for the PRET is the spectral overlap between the plasmon band of the metal and the absorption band of the semiconductor.<sup>63</sup> Based on the UV–vis spectra, such overlap does not exist in the Au@a-TiO<sub>2</sub> sample; the PRET mechanism is therefore not valid in the Au@a-TiO<sub>2</sub> case, narrowing the possible mechanism of charge transfer to the hot-carrier injection mechanism. The hot-carrier injection mechanism's precondition is the direct contact between the metal and the semiconductor, which is valid for the fabricated Au@a-TiO<sub>2</sub> sample.<sup>63</sup>

To provide evidence that a-TiO<sub>2</sub> is an integral entity in the Au@a-TiO<sub>2</sub> photoelectrode, two supplementary experiments were conducted. In the first measurement, the a-TiO<sub>2</sub> shell was replaced with Al<sub>2</sub>O<sub>3</sub> (Au@Al<sub>2</sub>O<sub>3</sub>). Figure S8a exhibits *i*–*t* curves of the Au@Al<sub>2</sub>O<sub>3</sub> under AM1.5G 1 sun and UV-filtered 1 sun illumination. It is evident that coating the surface with an insulator dramatically decreased the photocurrent. In the next experiment, the Au@a-TiO<sub>2</sub> was annealed at 500 °C to induce crystallinity. This sample was named Au@c-TiO<sub>2</sub>, and *i*–*t* curves of this sample for AM1.5G 1 sun and UV-filtered 1 sun

illumination are shown in Figure S8b. The Au@c-TiO<sub>2</sub> exhibited 1.75 and 0.25 mA cm<sup>-2</sup>, which is a large decrease in the PEC performance compared to the photocurrent values obtained using Au@a-TiO<sub>2</sub>. These experiments verify that the a-TiO<sub>2</sub> is an essential component in the Au@a-TiO<sub>2</sub>. Its amorphous nature facilitates hot hole harvesting in the Au@a-TiO<sub>2</sub> photoelectrode and dramatically enhances the photo-response of this electrode.

**2.4. Density Functional Theory Modeling Results.** To gain further insights into the band structure of the Au@a-TiO<sub>2</sub> photoelectrodes, density functional theory (DFT) calculations were performed for this heterostructure (see the materials and methods section in the Supporting Information for details of the DFT calculations). DFT is a powerful tool to gain insights into the projected density of states (PDOS) in the system under consideration.<sup>44</sup> In order to find the band structure of the heterojunction, the molecular orbitals are found for when Au and a-TiO<sub>2</sub> are a fair distance apart (“far” configuration) and for when Au and TiO<sub>2</sub> are in intimate contact (“close” configuration). Figure 5 depicts the PDOS of the simulated Au@a-TiO<sub>2</sub> heterostructure in intimate contact and the positions of highest occupied molecular orbital (HOMO) and lowest unoccupied molecular orbital (LUMO) of Au and a-TiO<sub>2</sub> in the far (Figure 5b) and close (Figure 5c) configurations. From Figure 5b, it is clear that in the far configuration, the HOMO and LUMO are both localized on Au NPs. In the close configuration, the LUMO is spread out on both Au and a-TiO<sub>2</sub>, while the HOMO level is mainly localized on Au NPs with small amount of penetration into the a-TiO<sub>2</sub> structure. Such spatial molecular orbital separation is indicative of superior charge separation following excitations. The PDOS calculations showed that a-TiO<sub>2</sub> valence and conduction bands are predominantly composed of oxygen p-orbitals and titanium d-orbitals (Figure 5a), consistent with the reported literature.<sup>64,65</sup> The PDOS calculations support the formation of defects inside the band gap of a-TiO<sub>2</sub> due to

perturbation and oxygen deficiencies.<sup>66</sup> For comparison purposes, the PDOS for an Au–TiO<sub>2</sub> heterostructure without any perturbation and oxygen vacancies was calculated (Figure S9a), which does not show any mid-gap defect states in crystalline TiO<sub>2</sub>. Figure S9b shows the orbital-resolved PDOS of Au. The occupied states of gold are mainly composed of d-orbitals, while states above the Fermi level are mostly sp-orbitals. The PDOS result also supports the transfer of photoexcited holes from the d band of Au to the defect states of a-TiO<sub>2</sub>. The Au 3d extends from –1.5 and –1 eV, and the sp hybridized orbital of Au extends from 0 to 0.6 eV. Based on the PDOS result, under visible light illumination, the electrons are photoexcited from Au 3d to Au sp, leaving holes behind in Au 3d levels which can get injected into a-TiO<sub>2</sub> by a defect-assisted process.

Surface scattering and chemical interface damping are particularly important decay channels for small (<20 nm) coinage metal NPs. For the moderately sized (~50 nm average diameter) Au NPs used in this work, surface scattering and chemical interface damping do not contribute significantly to plasmon dephasing.<sup>36</sup> Interband damping is the dominant damping mechanism in this size range. The mechanism of charge transfer under visible light illumination for both Au@a-TiO<sub>2</sub> and a-TiO<sub>2</sub>–Au configurations is depicted in Figure 6.

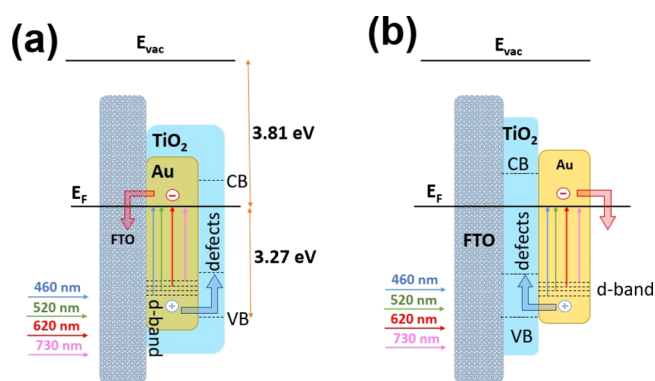


**Figure 6.** Proposed charge-transfer mechanism in (a) Au@a-TiO<sub>2</sub> and (b) a-TiO<sub>2</sub>–Au photoelectrodes.

Au is the primary light absorber since FTO is transparent to deep-UV wavelengths and the thickness of TiO<sub>2</sub> is limited to 10 nm. Regardless of the application of positive or negative bias to the photoelectrode, when Au@a-TiO<sub>2</sub> is under AM1.5G 1 sun illumination, it results in the creation of hot holes in the *d* band of Au NPs that are injected into the a-TiO<sub>2</sub> shell through defect states (Figure 6a). The holes in a-TiO<sub>2</sub> participate in oxidation reactions at the photoelectrode/electrolyte interface. The electrons in this process, which are formed near or above the Fermi level of Au, are injected into FTO and flow through the external circuit to the counter electrode (Pt electrode) and drive the reduction of protons. The remarkable PEC performance of the Au@a-TiO<sub>2</sub> architecture depicted in Figure 6a indicates it to be an excellent photoanode for the water-splitting reaction. For the a-TiO<sub>2</sub>–Au architecture (Figure 6b), under visible light irradiation and negative applied potential, a similar process occurs except that this architecture is a superior photocathode. Hot holes form in the *d*-band of Au. These holes get injected into the thin a-TiO<sub>2</sub> layer underneath the gold nanoislands and are subsequently transferred to FTO and the counter

electrode. Electrons accumulated in Au participate in the reduction reaction at the a-TiO<sub>2</sub>–Au/electrolyte interface. What is noteworthy is that Au injects hot holes into the a-TiO<sub>2</sub> layer in both cases. The entire focus of research in Au–TiO<sub>2</sub> heterojunctions has been on the extraction of hot electrons to such an extent that most studies in this area do not even consider the possibility of the injection of *d*-band hot holes formed in Au (upon plasmon decay) into TiO<sub>2</sub>.<sup>67</sup> In this context, we provide persuasive evidence for a hot hole injection from Au into TiO<sub>2</sub> through PEC performance data for different types of illumination, hole scavenger test, surface potential shifts under illumination, and DFT modeling. Using the steady-state *i*–*t* curves shown in Figure 3a, to estimate the steady-state incident-photon-to-electron conversion efficiency, it indicates near-unity quantum yields (see Section S2 in Supporting Information) at 0.6 V anodic bias (vs Ag/AgCl) for high-energy photons ( $\lambda < 420$  nm). Narang et al. point out in a recent paper that the measured steady-state charge collection efficiencies for hot-carrier plasmonic photovoltaic and PEC cells remain less than 1%.<sup>3</sup> The results in this work would therefore constitute one of the highest observed charge collection efficiencies in plasmonic PEC cells.

### 3. CONCLUSIONS

In conclusion, we present a potential solution to the long-standing problem of hot hole extraction from gold nanostructures. Our results demonstrate that a thin layer of a-TiO<sub>2</sub> can function both as a hole extraction layer and as a protective layer in PEC water-splitting photoelectrodes. This demonstration is contrary to the conventional understanding of TiO<sub>2</sub> exclusively being an excellent electron-accepting material. Highly stable, ultrathin Au@a-TiO<sub>2</sub> photoelectrodes were fabricated by sputtering Au followed by ALD deposition of a-TiO<sub>2</sub>. The Au@a-TiO<sub>2</sub> photoanodes generated an outstanding photocurrent of 2.5 mA cm<sup>-2</sup> under AM1.5G 1 sun illumination, which is almost 8.3 times higher than an ALD-deposited a-TiO<sub>2</sub> layer. Addition of a hole scavenger to the electrolyte resulted in the anodic photocurrent increasing to 3.7 mA cm<sup>-2</sup> for a photoanode with an overall thickness <100 nm. Such a remarkable PEC performance resulted from the successful extraction of hot holes from Au into a-TiO<sub>2</sub>. The Au@a-TiO<sub>2</sub> photoelectrode exhibited strong absorption in the visible part of the solar spectrum and enhanced photocurrent generation compared to the a-TiO<sub>2</sub> layer under visible light irradiation. Our work shows that near-unity charge collection efficiencies are achievable in hot-carrier-driven PEC cells for at least select spectral bands in sunlight, and that external quantum yields need not be limited to low single digit values in plasmonic catalysis.

### ■ ASSOCIATED CONTENT

#### Supporting Information

The Supporting Information is available free of charge at <https://pubs.acs.org/doi/10.1021/acsami.1c10698>.

Experimental and modeling methods; estimation of the quantum yield; additional FESEM images; XPS spectra and depth profile; additional PEC *i*–*v* and *i*–*t* curves; UPS spectra; Mott–Schottky plots; projected and orbital-resolved DOS; and gas chromatogram (PDF)

## ■ AUTHOR INFORMATION

## Corresponding Authors

Ehsan Vahidzadeh – Department of Electrical and Computer Engineering, University of Alberta, Edmonton, Alberta T6G 1H9, Canada; Email: vahidzad@ualberta.ca

Karthik Shankar – Department of Electrical and Computer Engineering, University of Alberta, Edmonton, Alberta T6G 1H9, Canada; [orcid.org/0000-0001-7347-3333](https://orcid.org/0000-0001-7347-3333); Email: kshankar@ualberta.ca

## Authors

Sheng Zeng – Department of Electrical and Computer Engineering, University of Alberta, Edmonton, Alberta T6G 1H9, Canada

Kazi M. Alam – Department of Electrical and Computer Engineering, University of Alberta, Edmonton, Alberta T6G 1H9, Canada; Nanotechnology Research Centre, National Research Council Canada, Edmonton, Alberta T6G 2M9, Canada; [orcid.org/0000-0001-5075-5928](https://orcid.org/0000-0001-5075-5928)

Pawan Kumar – Department of Electrical and Computer Engineering, University of Alberta, Edmonton, Alberta T6G 1H9, Canada; Present Address: Department of Chemical and Petroleum Engineering, University of Calgary, Calgary, AB, Canada T2N 1N4; [orcid.org/0000-0003-2804-9298](https://orcid.org/0000-0003-2804-9298)

Saralyn Riddell – Department of Electrical and Computer Engineering, University of Alberta, Edmonton, Alberta T6G 1H9, Canada

Narendra Chaulagain – Department of Electrical and Computer Engineering, University of Alberta, Edmonton, Alberta T6G 1H9, Canada

Sergey Gusarov – Nanotechnology Research Centre, National Research Council Canada, Edmonton, Alberta T6G 2M9, Canada; [orcid.org/0000-0003-2033-705X](https://orcid.org/0000-0003-2033-705X)

Alexander E. Kobryn – Nanotechnology Research Centre, National Research Council Canada, Edmonton, Alberta T6G 2M9, Canada

Complete contact information is available at: <https://pubs.acs.org/10.1021/acsami.1c10698>

## Author Contributions

The manuscript was written through contributions of all authors. All authors have given approval to the final version of the manuscript.

## Notes

The authors declare no competing financial interest.

## ■ ACKNOWLEDGMENTS

All authors thank NSERC and Future Energy Systems CFREF for financial support. Indirect (equipment related) support from the National Research Council Canada and the Canada Foundation for Innovation are acknowledged. E.V. acknowledges being part of, and receiving funding from, the Alberta-Technical University of Munich (ATUMS) collaborative training program, which is itself financially supported by NSERC (CREATE program), Alberta Innovates (Strategic Projects program), and DFG. The authors acknowledge use of the vacuum deposition and characterization facilities at the University of Alberta nanoFAB.

## ■ REFERENCES

- (1) Fujishima, A.; Honda, K. Electrochemical Photolysis of Water at a Semiconductor Electrode. *Nature* **1972**, *238*, 37–38.
- (2) Halmann, M. Photoelectrochemical Reduction of Aqueous Carbon Dioxide on p-type Gallium Phosphide in Liquid Junction Solar Cells. *Nature* **1978**, *275*, 115–116.
- (3) Cortés, E.; Besteiro, L. V.; Alabastri, A.; Baldi, A.; Tagliabue, G.; Demetriadou, A.; Narang, P. Challenges in Plasmonic Catalysis. *ACS Nano* **2020**, *14*, 16202–16219.
- (4) Araujo, T. P.; Quiroz, J.; Barbosa, E. C. M.; Camargo, P. H. C. Understanding Plasmonic Catalysis with Controlled Nanomaterials based on Catalytic and Plasmonic Metals. *Curr. Opin. Colloid Interface Sci.* **2019**, *39*, 110–122.
- (5) Manuel, A.; Shankar, K. Hot Electrons in TiO<sub>2</sub>–Noble Metal Nano-Heterojunctions: Fundamental Science and Applications in Photocatalysis. *Nanomaterials* **2021**, *11*, 1249.
- (6) Wei, R.-B.; Kuang, P.-Y.; Cheng, H.; Chen, Y.-B.; Long, J.-Y.; Zhang, M.-Y.; Liu, Z.-Q. Plasmon-Enhanced Photoelectrochemical Water Splitting on Gold Nanoparticle Decorated ZnO/CdS Nanotube Arrays. *ACS Sustain. Chem. Eng.* **2017**, *5*, 4249–4257.
- (7) Zheng, B.-F.; Ouyang, T.; Wang, Z.; Long, J.; Chen, Y.; Liu, Z.-Q. Enhanced Plasmon-Driven Photoelectrocatalytic Methanol Oxidation on Au Decorated  $\alpha$ -Fe<sub>2</sub>O<sub>3</sub> Nanotube Arrays. *Chem. Commun.* **2018**, *54*, 9583–9586.
- (8) Ishii, S.; Shinde, S. L.; Nagao, T. Nonmetallic Materials for Plasmonic Hot Carrier Excitation. *Adv. Opt. Mater.* **2019**, *7*, 1800603.
- (9) Karaballi, R. A.; Monfared, Y. E.; Dasog, M. Overview of Synthetic Methods to Prepare Plasmonic Transition-Metal Nitride Nanoparticles. *Chem.—Eur. J.* **2020**, *26*, 8499–8505.
- (10) Farsinezhad, S.; Shanavas, T.; Mahdi, N.; Askar, A. M.; Kar, P.; Sharma, H.; Shankar, K. Core-Shell Titanium Dioxide-Titanium Nitride Nanotube Arrays with Near-Infrared Plasmon Resonances. *Nanotechnology* **2018**, *29*, 154006.
- (11) Hubenthal, F. Increased Damping of Plasmon Resonances in Gold Nanoparticles Due to Broadening of the Band Structure. *Plasmonics* **2013**, *8*, 1341–1349.
- (12) Manuel, A. P.; Kirkey, A.; Mahdi, N.; Shankar, K. Plexcitonics - Fundamental Principles and Optoelectronic Applications. *J. Mater. Chem. C* **2019**, *7*, 1821–1853.
- (13) Sundararaman, R.; Narang, P.; Jermyn, A. S.; Goddard, W. A., III; Atwater, H. A. Theoretical Predictions for Hot-Carrier Generation from Surface Plasmon Decay. *Nat. Commun.* **2014**, *5*, 5788.
- (14) Aslam, U.; Chavez, S.; Lincic, S. Controlling Energy Flow in Multimetallic Nanostructures for Plasmonic Catalysis. *Nat. Nanotechnol.* **2017**, *12*, 1000.
- (15) Harutyunyan, H.; Martinson, A. B. F.; Rosenmann, D.; Khorashad, L. K.; Besteiro, L. V.; Govorov, A. O.; Wiederrecht, G. P. Anomalous Ultrafast Dynamics of Hot Plasmonic Electrons in Nanostructures with Hot Spots. *Nat. Nanotechnol.* **2015**, *10*, 770–774.
- (16) Wang, M.; Ye, M.; Iocozzia, J.; Lin, C.; Lin, Z. Plasmon-Mediated Solar Energy Conversion via Photocatalysis in Noble Metal/Semiconductor Composites. *Adv. Sci.* **2016**, *3*, 1600024.
- (17) Alam, K. M.; Kumar, P.; Manuel, A. P.; Vahidzadeh, E.; Goswami, A.; Zeng, S.; Wu, W. J.; Mahdi, N.; Cui, K.; Kobryn, A. E.; Gusarov, S.; Song, Y. N.; Shankar, K. CVD Grown Nitrogen Doped Graphene is an Exceptional Visible-Light Driven Photocatalyst for Surface Catalytic Reactions. *2D Mater.* **2019**, *7*, 015002.
- (18) Zeng, S.; Vahidzadeh, E.; VanEssen, C. G.; Kar, P.; Kisslinger, R.; Goswami, A.; Zhang, Y.; Mandi, N.; Riddell, S.; Kobryn, A. E.; Gusarov, S.; Kumar, P.; Shankar, K. Optical control of selectivity of high rate CO<sub>2</sub> photoreduction via interband or hot electron Z-scheme reaction pathways in Au-TiO<sub>2</sub> plasmonic photonic crystal photocatalyst. *Appl. Catal., B* **2020**, *267*, 118644.
- (19) Kisslinger, R.; Riddell, S.; Manuel, A. P.; Alam, K. M.; Kalra, A. P.; Cui, K.; Shankar, K. Nonlithographic Formation of Ta<sub>2</sub>O<sub>5</sub> Nanodimple Arrays Using Electrochemical Anodization and Their Use in Plasmonic Photocatalysis for Enhancement of Local Field and Catalytic Activity. *ACS Appl. Mater. Interfaces* **2021**, *13*, 4340–4351.

- (20) Vahidzadeh, E.; Zeng, S.; Manuel, A. P.; Riddell, S.; Kumar, P.; Alam, K. M.; Shankar, K. Asymmetric Multipole Plasmon-Mediated Catalysis Shifts the Product Selectivity of CO<sub>2</sub> Photoreduction toward C<sub>2</sub>+ Products. *ACS Appl. Mater. Interfaces* **2021**, *13*, 7248–7258.
- (21) Pan, H.; Steiniger, A.; Heagy, M. D.; Chowdhury, S. Efficient Production of Formic Acid by Simultaneous Photoreduction of Bicarbonate and Oxidation of Glycerol on Gold-TiO<sub>2</sub> Composite Under Solar Light. *J. CO<sub>2</sub> Util.* **2017**, *22*, 117–123.
- (22) Wang, M.; Pang, X.; Zheng, D.; He, Y.; Sun, L.; Lin, C.; Lin, Z. Nonepitaxial Growth of Uniform and Precisely Size-Tunable Core/Shell Nanoparticles and their Enhanced Plasmon-Driven Photocatalysis. *J. Mater. Chem. A* **2016**, *4*, 7190–7199.
- (23) Ishida, T.; Toe, S.; Tatsuma, T. Stepwise Injection of Energetic Electrons and Holes in Plasmon-Induced Charge Separation. *J. Phys. Chem. C* **2019**, *123*, 30562–30570.
- (24) Smith, K. A.; Savva, A. I.; Deng, C.; Wharry, J. P.; Hwang, S.; Su, D.; Wang, Y.; Gong, J.; Xu, T.; Butt, D. P.; Xiong, H. Effects of Proton Irradiation on Structural and Electrochemical Charge Storage Properties of TiO<sub>2</sub> Nanotube Electrodes for Lithium-Ion Batteries. *J. Mater. Chem. A* **2017**, *5*, 11815–11824.
- (25) Niilisk, A.; Moppel, M.; Pärs, M.; Sildos, I.; Jantson, T.; Avarmaa, T.; Jaaniso, R.; Aarik, J. Structural Study of TiO<sub>2</sub> Thin Films by Micro-Raman Spectroscopy. *Open Phys.* **2006**, *4*, 105–116.
- (26) Ghobadi, A.; Ulusoy, T. G.; Garifullin, R.; Guler, M. O.; Okyay, A. K. A Heterojunction Design of Single Layer Hole Tunneling ZnO Passivation Wrapping Around TiO<sub>2</sub> Nanowires for Superior Photocatalytic Performance. *Sci. Rep.* **2016**, *6*, 30587.
- (27) Ulusoy, T. G.; Ghobadi, A.; Okyay, A. K. Surface Engineered Angstrom Thick ZnO-Sheathed TiO<sub>2</sub> Nanowires as Photoanodes for Performance Enhanced Dye-Sensitized Solar Cells. *J. Mater. Chem. A* **2014**, *2*, 16867–16876.
- (28) Zhu, L.; Zeng, Y.; Zhang, S.; Deng, J.; Zhong, Q. Effects of Synthesis Methods on Catalytic Activities of CoO<sub>x</sub>-TiO<sub>2</sub> For Low-Temperature NH<sub>3</sub>-SCR of NO. *J. Environ. Sci.* **2017**, *54*, 277–287.
- (29) Olowoyo, J. O.; Kumar, M.; Dash, T.; Saran, S.; Bhandari, S.; Kumar, U. Self-Organized Copper Impregnation and Doping in TiO<sub>2</sub> with Enhanced Photocatalytic Conversion of H<sub>2</sub>O and CO<sub>2</sub> to Fuel. *Int. J. Hydrogen Energy* **2018**, *43*, 19468–19480.
- (30) Kim, M.-S.; Chung, S.-H.; Yoo, C.-J.; Lee, M. S.; Cho, I.-H.; Lee, D.-W.; Lee, K.-Y. Catalytic Reduction of Nitrate in Water over Pd-Cu/TiO<sub>2</sub> Catalyst: Effect of the Strong Metal-Support Interaction (SMSI) on the Catalytic Activity. *Appl. Catal., B* **2013**, *142–143*, 354–361.
- (31) Wu, L.; Li, F.; Xu, Y.; Zhang, J. W.; Zhang, D.; Li, G.; Li, H. Plasmon-Induced Photoelectrocatalytic Activity of Au Nanoparticles Enhanced TiO<sub>2</sub> Nanotube Arrays Electrodes for Environmental Remediation. *Appl. Catal., B* **2015**, *164*, 217–224.
- (32) Hoang, C. V.; Hayashi, K.; Ito, Y.; Gorai, N.; Allison, G.; Shi, X.; Sun, Q.; Cheng, Z.; Ueno, K.; Goda, K.; Misawa, H. Interplay of Hot Electrons from Localized and Propagating Plasmons. *Nat. Commun.* **2017**, *8*, 771.
- (33) Moehl, T.; Suh, J.; Sévery, L.; Wick-Joliat, R.; Tilley, S. D. Investigation of (Leaky) ALD TiO<sub>2</sub> Protection Layers for Water-Splitting Photoelectrodes. *ACS Appl. Mater. Interfaces* **2017**, *9*, 43614–43622.
- (34) Amano, F. Photoelectrochemical Oxygen Evolution. *Solar-to-Chemical Conversion*; Wiley, 2021; pp 163–187.
- (35) Kumar, P.; Kar, P.; Manuel, A. P.; Zeng, S.; Thakur, U. K.; Alam, K. M.; Zhang, Y.; Kisslinger, R.; Cui, K.; Bernard, G. M.; Michaelis, V. K.; Shankar, K. Noble Metal Free, Visible Light Driven Photocatalysis Using TiO<sub>2</sub> Nanotube Arrays Sensitized by P-Doped C<sub>3</sub>N<sub>4</sub> Quantum Dots. *Adv. Opt. Mater.* **2020**, *8*, 1901275.
- (36) Pinchuk, A.; Von Plessen, G.; Kreibitz, U. Influence of Interband Electronic Transitions on the Optical Absorption in Metallic Nanoparticles. *J. Phys. D: Appl. Phys.* **2004**, *37*, 3133.
- (37) Abb, M.; Albella, P.; Aizpurua, J.; Muskens, O. L. All-Optical Control of a Single Plasmonic Nanoantenna-ITO Hybrid. *Nano Lett.* **2011**, *11*, 2457–2463.
- (38) Cushing, S. K.; Chen, C.-J.; Dong, C. L.; Kong, X.-T.; Govorov, A. O.; Liu, R.-S.; Wu, N. Tunable Nonthermal Distribution of Hot Electrons in a Semiconductor Injected from a Plasmonic Gold Nanostructure. *ACS Nano* **2018**, *12*, 7117–7126.
- (39) Sreedhar, A.; Reddy, I. N.; Kwon, J. H.; Yi, J.; Sohn, Y.; Gwag, J. S.; Noh, J.-S. Charge Carrier Generation and Control on Plasmonic Au Clusters Functionalized TiO<sub>2</sub> Thin Films for Enhanced Visible Light Water Splitting Activity. *Ceram. Int.* **2018**, *44*, 18978–18986.
- (40) Zorić, I.; Zäch, M.; Kasemo, B.; Langhammer, C. Gold, Platinum, and Aluminum Nanodisk Plasmons: Material Independence, Subradiance, and Damping Mechanisms. *ACS Nano* **2011**, *5*, 2535–2546.
- (41) Tan, F.; Li, T.; Wang, N.; Lai, S. K.; Tsoi, C. C.; Yu, W.; Zhang, X. Rough Gold Films as Broadband Absorbers for Plasmonic Enhancement of TiO<sub>2</sub> Photocurrent Over 400–800 nm. *Sci. Rep.* **2016**, *6*, 33049.
- (42) Nishi, H.; Tatsuma, T. Mechanistic Analysis of Plasmon-Induced Charge Separation by the Use of Chemically Synthesized Gold Nanorods. *J. Phys. Chem. C* **2018**, *122*, 2330–2335.
- (43) Jian, A.; Feng, K.; Jia, H.; Zhang, Q.; Sang, S.; Zhang, X. Quantitative Investigation of Plasmonic Hot-Electron Injection by KPFM. *Appl. Surf. Sci.* **2019**, *492*, 644–650.
- (44) Zeng, S.; Vahidzadeh, E.; VanEssen, C. G.; Kar, P.; Kisslinger, R.; Goswami, A.; Zhang, Y.; Mahdi, N.; Riddell, S.; Kobryn, A. E.; Gusarov, S.; Kumar, P.; Shankar, K. Optical Control of Selectivity of High Rate CO<sub>2</sub> Photoreduction Via Interband-or Hot Electron Z-Scheme Reaction Pathways in Au-TiO<sub>2</sub> Plasmonic Photonic Crystal Photocatalyst. *Appl. Catal., B* **2020**, *267*, 118644.
- (45) Guzman, F.; Chuang, S. S.; Yang, C. Role of Methanol Sacrificing Reagent in the Photocatalytic Evolution of Hydrogen. *Ind. Eng. Chem. Res.* **2013**, *52*, 61–65.
- (46) Kalamaras, E.; Lianos, P. Current Doubling Effect Revisited: Current Multiplication in a PhotoFuelCell. *J. Electroanal. Chem.* **2015**, *751*, 37–42.
- (47) Halevy, S.; Korin, E.; Bettelheim, A. Enhancement of Photoelectrochemical Organics Degradation and Power Generation by Electrodeposited Coatings of g-C<sub>3</sub>N<sub>4</sub> and Graphene on TiO<sub>2</sub> Nanotube Arrays. *Nanoscale Adv.* **2019**, *1*, 4128–4136.
- (48) Zariifi, M. H.; Farsinezhad, S.; Abdolrazzagh, M.; Daneshmand, M.; Shankar, K. Selective Microwave Sensors Exploiting the Interaction of Analytes with Trap States in TiO<sub>2</sub> Nanotube Arrays. *Nanoscale* **2016**, *8*, 7466–7473.
- (49) Tamaki, Y.; Furube, A.; Murai, M.; Hara, K.; Katoh, R.; Tachiya, M. Direct Observation of Reactive Trapped Holes in TiO<sub>2</sub> Undergoing Photocatalytic Oxidation of Adsorbed Alcohols: Evaluation of the Reaction Rates and Yields. *J. Am. Chem. Soc.* **2006**, *128*, 416–417.
- (50) Farsinezhad, S.; Banerjee, S. P.; Rajeeva, B. B.; Wiltshire, B. D.; Sharma, H.; Sura, A.; Mohammadpour, A.; Kar, P.; Fedosejevs, R.; Shankar, K. Reduced Ensemble Plasmon Line Widths and Enhanced Two-Photon Luminescence in Anodically Formed High Surface Area Au-TiO<sub>2</sub> 3D Nanocomposites. *ACS Appl. Mater. Interfaces* **2017**, *9*, 740–749.
- (51) Zhan, Z.; An, J.; Zhang, H.; Hansen, R. V.; Zheng, L. Three-Dimensional Plasmonic Photoanodes Based on Au-Embedded TiO<sub>2</sub> Structures for Enhanced Visible-Light Water Splitting. *ACS Appl. Mater. Interfaces* **2014**, *6*, 1139–1144.
- (52) Ratchford, D. C.; Dunkelberger, A. D.; Vurgaftman, I.; Owrutsky, J. C.; Pehrsson, P. E. Quantification of Efficient Plasmonic Hot-Electron Injection in Gold Nanoparticle-TiO<sub>2</sub> Films. *Nano Lett.* **2017**, *17*, 6047–6055.
- (53) Hangleiter, A.; Häcker, R. Enhancement of Band-to-Band Auger Recombination by Electron-Hole Correlations. *Phys. Rev. Lett.* **1990**, *65*, 215–218.
- (54) Farsinezhad, S.; Sharma, H.; Shankar, K. Interfacial Band Alignment for Photocatalytic Charge Separation in TiO<sub>2</sub> Nanotube Arrays Coated with CuPt Nanoparticles. *Phys. Chem. Chem. Phys.* **2015**, *17*, 29723–29733.

(55) King, D. M.; Du, X.; Cavanagh, A. S.; Weimer, A. W. Quantum Confinement in Amorphous TiO<sub>2</sub> Films Studied Via Atomic Layer Deposition. *Nanotechnology* **2008**, *19*, 445401.

(56) Nisika, K.; Kaur, K.; Arora, K.; Chowdhury, A. H.; Bahrami, B.; Qiao, Q.; Kumar, M. Energy Level Alignment and Nanoscale Investigation of a-TiO<sub>2</sub>/Cu-Zn-Sn-S Interface for Alternative Electron Transport Layer in Earth Abundant Cu-Zn-Sn-S Solar Cells. *J. Appl. Phys.* **2019**, *126*, 193104.

(57) Cameron, D. C.; Krumpolec, R.; Ivanova, T. V.; Homola, T.; Černák, M. Nucleation and Initial Growth of Atomic Layer Deposited Titanium Oxide Determined by Spectroscopic Ellipsometry and the Effect of Pretreatment by Surface Barrier Discharge. *Appl. Surf. Sci.* **2015**, *345*, 216–222.

(58) Zarifi, M. H.; Mohammadpour, A.; Farsinezhad, S.; Wiltshire, B. D.; Nosrati, M.; Askar, A. M.; Daneshmand, M.; Shankar, K. Time-Resolved Microwave Photoconductivity (TRMC) Using Planar Microwave Resonators: Application to the Study of Long-Lived Charge Pairs in Photoexcited Titania Nanotube Arrays. *J. Phys. Chem. C* **2015**, *119*, 14358–14365.

(59) Dominici, L.; Michelotti, F.; Brown, T. M.; Reale, A.; Carlo, A. D. Plasmon Polaritons in the Near Infrared on Fluorine Doped Tin Oxide Films. *Opt. Express* **2009**, *17*, 10155–10167.

(60) Kendall, O.; Wainer, P.; Barrow, S.; van Embden, J.; Della Gaspera, E. Fluorine-Doped Tin Oxide Colloidal Nanocrystals. *Nanomaterials* **2020**, *10*, 863.

(61) Wu, X.; Centeno, A.; Zhang, X.; Darvill, D.; Ryan, M. P.; Riley, D. J.; Alford, N. M.; Xie, F. Broadband Plasmon Photocurrent Generation from Au Nanoparticles/Mesoporous TiO<sub>2</sub> Nanotube Electrodes. *Sol. Energy Mater. Sol. Cells* **2015**, *138*, 80–85.

(62) Warren, S. C.; Thimsen, E. Plasmonic Solar Water Splitting. *Energy Environ. Sci.* **2012**, *5*, 5133–5146.

(63) Cushing, S. K.; Li, J.; Bright, J.; Yost, B. T.; Zheng, P.; Bristow, A. D.; Wu, N. Controlling Plasmon-Induced Resonance Energy Transfer and Hot Electron Injection Processes in Metal@TiO<sub>2</sub> Core-Shell Nanoparticles. *J. Phys. Chem. C* **2015**, *119*, 16239–16244.

(64) Pham, H. H.; Wang, L.-W. Oxygen Vacancy and Hole Conduction in Amorphous TiO<sub>2</sub>. *Phys. Chem. Chem. Phys.* **2015**, *17*, 541–550.

(65) Gutiérrez Moreno, J. J.; Nolan, M. Ab Initio Study of the Atomic Level Structure of the Rutile TiO<sub>2</sub> (110)–Titanium Nitride (TiN) Interface. *ACS Appl. Mater. Interfaces* **2017**, *9*, 38089–38100.

(66) Pan, X.; Yang, M.-Q.; Fu, X.; Zhang, N.; Xu, Y.-J. Defective TiO<sub>2</sub> with Oxygen Vacancies: Synthesis, Properties and Photocatalytic Applications. *Nanoscale* **2013**, *5*, 3601–3614.

(67) Yu, Y.; Wijesekera, K. D.; Xi, X.; Willets, K. A. Quantifying Wavelength-Dependent Plasmonic Hot Carrier Energy Distributions at Metal/Semiconductor Interfaces. *ACS Nano* **2019**, *13*, 3629–3637.